Chapter 1

MODEL COMPONENTS OF THE CERTIFICATION FRAMEWORK FOR GEOLOGIC CARBON SEQUESTRATION RISK ASSESSMENT

Curtis M. Oldenburg[1], Steven L. Bryant[2], Jean-Philippe Nicot[3], Navanit Kumar[2,5], Yingqi Zhang[1], Preston Jordan[1], Lehua Pan[1], Patrick Granvold[4], Fotini K. Chow[4]

[1]Earth Sciences Division, 90-1116, 1 Cyclotron Rd., Lawrence Berkeley National Laboratory, Berkeley CA 94720

[2]Department of Petroleum and Geosystems Engineering, The University of Texas at Austin, 1 University Station C0300, Austin, TX 78712

[3]Bureau of Economic Geology, Jackson School of Geosciences, The University of Texas at Austin, University Station, Box X, Austin, Texas 78713

[4]Department of Civil and Environmental Engineering, University of California, Berkeley, Berkeley, CA 94720

[5]Shell Oil and Production Company, 200 North Dairy Ashford, Houston, TX 77079

ABSTRACT: We have developed a framework for assessing the leakage risk of geologic carbon sequestration sites. This framework, known as the Certification Framework (CF), emphasizes wells and faults as the primary potential leakage conduits. Vulnerable resources are grouped into compartments, and impacts due to leakage are quantified by the leakage flux or concentrations that could potentially occur in compartments under various scenarios. The CF utilizes several model components to simulate leakage scenarios. One model component is a catalog of results of reservoir simulations that can be queried to estimate plume travel distances and times, rather than requiring CF users to run new reservoir simulations for each case. Other model components developed for the CF and described here include fault characterization using fault-population statistics; fault connection probability using fuzzy rules; well-flow modeling with a drift-flux model implemented in TOUGH2; and atmospheric dense-gas dispersion using a mesoscale weather prediction code.

INTRODUCTION

We have developed a novel and practical risk-based framework for certifying that the leakage risk of a potential geologic carbon sequestration (GCS) site is below agreed-upon thresholds [1, 2, 3]. The approach we developed, known as the Certification Framework (CF), proposes a standardized way for project proponents, regulators, and the public to analyze and understand risks and uncertainties of GCS in a simple and transparent way. The CF goes beyond the scope of regulations of deep underground injection permitted by the U.S. Environmental Protection Agency (EPA) which protect underground sources of drinking water (USDW) to consider risks to a broader set of resources and environmental assets as well as loss of emission-reduction credits due to CO_2 leakage. The CF uses physically grounded models for the movement of injected CO_2 and brine, and for assessing the likelihood that CO_2 or injection-related pressure perturbation will intersect wells and faults. The CF and an example case study have been fully described elsewhere [3]. This paper describes the essential model components that we have developed for carrying out a CF analysis. These model components include the catalog of simulation results, fault population statistics, fault connectivity analyses, well-bore flow, and dense gas dispersion.

BRIEF OVERVIEW OF THE CF

The goal of the CF is to evaluate the degree to which a GCS site is expected to be safe and effective. In the risk-assessment context, the word "safe" means that impacts to humans and other living things, the environment, and other resources resulting from injection are acceptably low over both short and long time periods. The word "effective" means that the site will contain indefinitely the vast majority of injected CO_2 [4]. The approach we take in the CF is to simplify the system into a tractable and logical form amenable to modeling and analysis. We achieve simplicity in the CF by assuming that sedimentary basins share common concerns such as the presence of wells and faults as potential leakage pathways.

The CF uses the concept of "effective trapping" [3] in acknowledgment of the enormous volumes of CO_2 that will be injected into the non-leak-proof deep subsurface. If small amounts of injected CO_2 escape to the atmosphere, the net mitigation of CO_2 emissions is still substantial. Furthermore, effective trapping is intended to recognize the fact that migration of injected CO_2 can significantly increase the amount stored in secure forms (e.g., dissolved in brine, or trapped as a residual phase) [5]. Of course, harmful leakage of CO_2 (or brine) into USDW, into other resources, or even out of the ground is also possible. Analyses with the CF distinguish benign from harmful migration so that the risk management can focus on the latter.

The CF approach uses a precise terminology. Before leakage of CO_2 can be discussed, it must be defined. To this end, the following definitions are established:

- *Effective Trapping* is the proposed overarching requirement for safety and effectiveness.
- *Storage Region* is the three-dimensional volume of the subsurface intended to contain injected CO_2.
- *Leakage* is migration across the boundary of the Storage Region.
- *Compartment* is a collection of vulnerable entities (e.g., environment and resources).
- *Impact* is a consequence to a compartment, evaluated by proxy concentrations or fluxes.
- *Risk* is the product of probability and consequence (impact).
- *CO_2 Leakage Risk* is the product of the probability and negative impact to compartments arising from CO_2 migration.
- *Effective Trapping* is achieved if CO_2 Leakage Risk is below agreed-upon thresholds.

The purpose of the CF is to evaluate the CO_2 Leakage Risk (CLR) for each compartment to determine whether the Effective Trapping threshold will be met for a proposed GCS site. Given the large amounts of brine that will be pressurized and displaced by injected CO_2, we further define the brine leakage risk (BLR) as the product of the probability and consequences to compartments of brine migration.

Wells and Faults are the Conduits

We assume in the CF that wells and faults are the only potential leakage conduits. This assumption is made to simplify the analysis and is predicated on the assumption that GCS sites will be well chosen so as to avoid sites with potentially discontinuous cap-rock seals. Under this assumption, the injected CO_2 and the associated over-pressured brine comprise the source of fluids that can potentially leak through the conduits.

Impacts Occur to Compartments

The consequence of upward leakage of CO_2 or brine is impact to compartments, which the CF uses to represent the vulnerable entities. For example, USDW, taken collectively at a site, forms a single compartment. In the CF, we define five compartments in which impacts will be evaluated.

- ECA = Emission Credits and Atmosphere
- HS = Health and Safety
- NSE = Near-Surface Environment
- USDW = Underground Source of Drinking Water
- HMR = Hydrocarbon and Mineral Resources

The compartments have general locations within the system but are abstract in the sense that they are collections and may include disconnected pieces. For example, there may be multiple zones of USDW and yet the CF would consider only one USDW compartment. Similarly, the HS compartment is abstract in that safety could refer to both a resident in a home or a worker in an office building. The ECA compartment is even more abstract in that emission credits are not physical entities.

We present in Figure 1a a cross section of a generic GCS site showing a deep structure potentially suitable for use in sequestering CO_2, sealing formations, an oil-bearing formation, faults, wells, USDW, vegetation, and a residence with water well. This conceptualization of common elements of a GCS system is further abstracted to consist of the source, conduits, and compartments of Figure 1b. In summary, the CF simplifies the GCS system so that the CO_2 (and brine) form a potential source of hazard, wells and faults comprise the potential leakage pathways, and impacts occur to compartments.

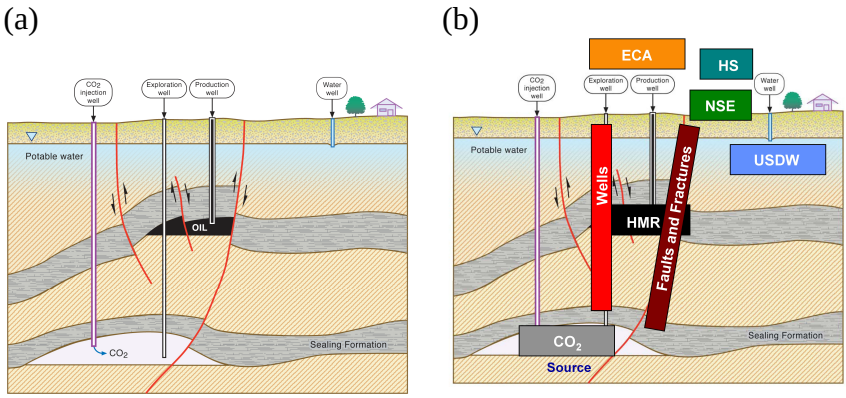

Figure 1. (a) Generic geologic cross section of potential GCS site showing reservoir and sealing formations, faults, wells, USDW, and near-surface and surface environments. (b) Generic cross section with CF source and compartments overlaid.

Evaluating Impacts

Impacts of CO_2 to compartments are evaluated by modeling and simulation of proxy concentrations or fluxes. The CF assumes that there are established limits on CO_2 or brine concentrations within the compartment as a whole, or on fluxes into the compartment, that ensure acceptable impact to the

compartment. The numerical value of these limits will be specified in regulations that may vary by country. Whether a concentration- or flux-based limit is appropriate depends on the context and compartment. For example, for modeling CO_2 impact to the HS compartment, it may be most convenient to set a concentration-based limit since the safety standards for CO_2 exposure are given in terms of concentration of CO_2 in air. In contrast, the ECA compartment impacts will be best modeled using a flux-based limit. In all cases, the time over which the high concentration or flux persists is important to calculate the associated impact. Reservoir simulation results (e.g., from a catalog of pre-computed results) are used to calculate fluxes and concentrations resulting from the CO_2 source and brine displacement process, and well and fault flow models are used for leakage up the conduits.

Likelihood of Impact and Risk

The CF uses the likelihood of intersection of the CO_2 (or brine) source with a conduit, and the likelihood of intersection of the conduit and a compartment to generate the probability of the given source-to-compartment leakage scenario. The risk associated with that leakage is the product of the likelihood of leakage and the impact of that leakage event. Acceptable risks from CO_2 or brine leakage will be those below a threshold provided by external sources such as regulators or carbon credit insurers.

Work Flow

The overall work flow of the CF approach is summarized in Figure 2. External inputs are required to characterize the site and define the reservoir, injection plan, and time frame. These inputs constrain the conditions and properties needed to estimate the CO_2 (source) plume location, footprint size, and pressure perturbation, e.g., by reservoir simulation. These characteristics of the plume change during injection and after injection ends. Values at times deemed significant by regulators, e.g. at end of injection, 25 yr and 100 yr after injection ends, can be extracted from the simulations. Next the CF uses external inputs on wells and faults, typically the plan-view spatial density of abandoned wells and conductive faults. The likelihood of the plume intersecting the conduits is a function of the plume size and conduit spatial density. The output of the reservoir simulation is fed to the conduit flow model to calculate fluxes and/or concentrations within compartments under the assumption that they intersect. The fluxes and/or concentrations calculated by the CF either exceed the limit or fall below the limit (are not impacts). The risk can then be calculated as the product of the impact and the likelihood of the corresponding intersection with conduits (leakage scenario). Comparing the calculated CLR to the externally provided threshold, the CF determines whether the leakage risk is acceptable. If the CLR is above the threshold, changes to the injection plan or refinements in site characterization may be made, resulting in decreased CLR. Although written in terms of CLR for brevity, the CF analysis of BLR follows the same flow process. Greater detail of the CF and a case study can be found in [3].

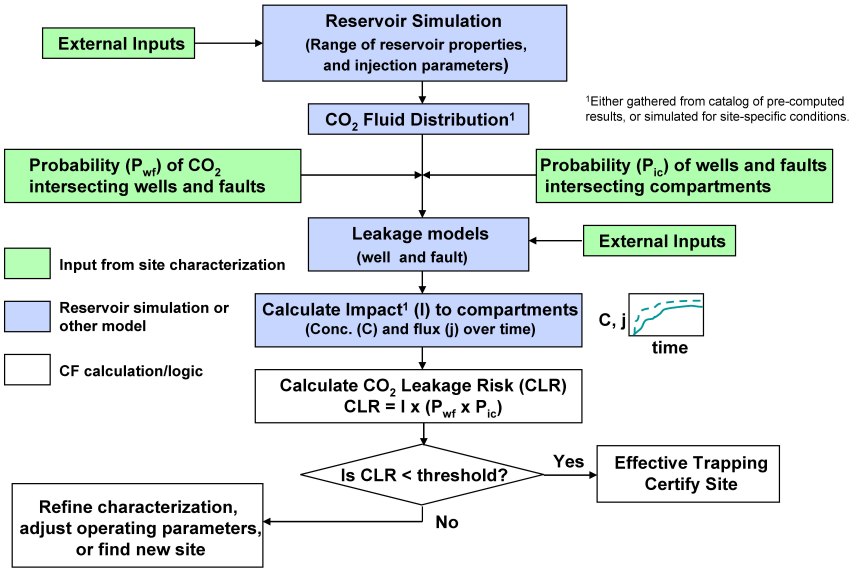

Figure 2. Flow chart of CF-CLR process showing logic and inputs and outputs.

As outlined above, the CF relies on model components and approaches for calculating risk. Specifically, physical process models (reservoir simulation, conduit leakage flow, and atmospheric dispersion) and model approaches (fault density, likelihood of fault intersection) are required to carry out a CF analysis. In the remainder of this chapter, we describe the five critical model components that we have developed for use in the CF. These components are particular examples for demonstration and application of the CF approach. Any of them could be replaced with a functionally equivalent model or approach without changing the fundamental framework or workflow of the CF.

MODEL COMPONENTS IN THE CF

Simulation Catalog

To facilitate use of the CF by a wide range of people, we have developed a catalog of reservoir simulation results that can be queried by users to obtain estimates of plume size and pressure perturbation at various times [6]. The reservoir simulations in the catalog were carried out using the CMG-GEM (Computer Modelling Group (Calgary), Generalized Equation of state Model) numerical reservoir simulator with the equation of state tuned to the CO_2/brine system [7, 8]. A large number of cases were simulated with a range of combinations of key reservoir properties such as thickness, dip, porosity, permeability, permeability anisotropy, injection interval, and injection rate. In the simulations, constant-rate injection is specified at the center of the generic model reservoirs, with constant-pressure conditions imposed at the model boundaries. The significant output extracted from the simulations and stored in the catalog includes time for CO_2 to migrate to the top of the reservoir, size of CO_2 plume and fraction of the CO_2 that is still mobile as functions of time, and pressure in the reservoir.

Parameter Ranges

Ranges of parameters for typical saline formation targets are presented in Table 1. As the initial attempt to construct such a catalog, simulations were carried out on a subset of these parameters indicated by shading in the table. The output is post-processed to provide a much reduced dataset in terms of the response variables for use in the CF. The risk parameters (time to hit top, maximum lateral extent, and total mobile gas) can be extracted from these simulations and interpolated for cases that do not exactly match catalog input parameters [9].

Table 1. Formation and operating parameters and their general range of values for aquifers. Shaded terms were used in this study.

FORMATION ROCK/FLUID PROPERTIES		Units	Range of values		
			High	Medium	Low
Anisotropy	k_v/k_h	--	1	0.03	0.001
Residual nonwetting phase saturation	$S_{g,r}$	--	0.8	0.5	0.2
Average saturation of CO_2 between injection well and injection front	S_{mean}	--	1	0.6	0.2
Relative permeability of CO_2 at displacement front	$k_{CO2,disp}$	--	1	0.5	0.1
Lateral correlation length of permeability	λ	m	∞ (layered)	100	0 (uncorrelated)
Dip angle (from horizontal)	α	°	20	5	0
Thickness	h	m	300	50	10
Average permeability (horizontal)	$<k_h>$	mD	1000	100	10
Average porosity	ϕ	--	0.40	0.20	0.10
Spacing of natural fractures (see spacing of faults)	w_{frac}	m	∞ (unfractured)	100	1
Fault permeability relative to matrix permeability	k_{fault}/k_h	--	100	1	0.01
FORMATION CHARACTERISTICS					
Depth	Z	m	3000	1000	100
Spacing of existing wells	w_{well}	m	∞ (no wells)	500	50
Spacing of faults	w_{fault}	m	∞ (no faults)	1000	100
Lateral distance from injector to top of nearest anticline	L	m	∞ (no structure)	2000	200
Thickness of caprock	h_{cap}	m	1000	100	10
OPERATIONAL PARAMETERS					
Number of vertical injection wells	N_{vert}	--	10	1	0
Number of horizontal injection wells	N_{horiz}	--	10	1	0
Mass of CO_2 to be injected	M	ton	10^8	10^7	10^6
Injection period	t_{inj}	y	50	10	5
Fraction of formation thickness in which vertical well is completed	f_{perf}	--	1	0.5	0.25

Response Variables

To constrain the CO_2 leakage potential, we consider the three response variables illustrated in Figure 3, namely (1) total mobile CO_2 in the aquifer, (2) maximum lateral distance traveled from the injector, and (3) time the plume takes to reach the top seal

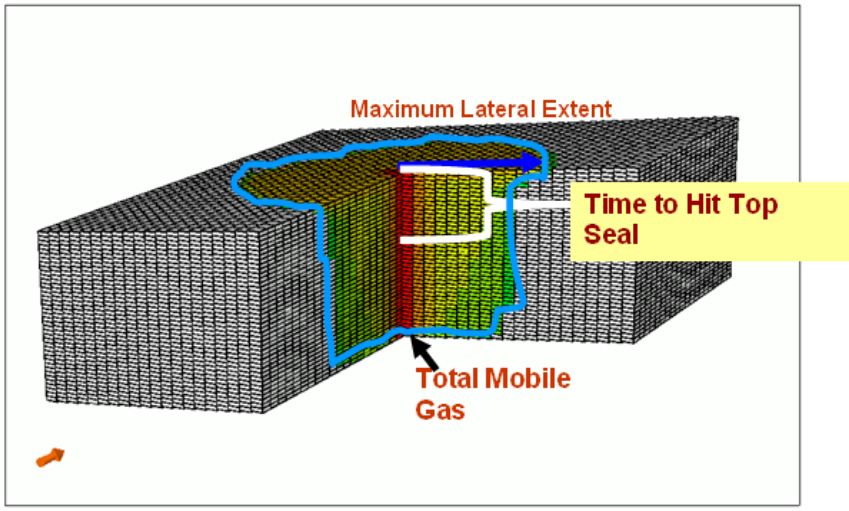

Figure 3. Schematic showing aquifer system with a vertical injector in center. Well is perforated in bottom half section of thickness. Three response variables (time to hit top seal, maximum lateral extent and total mobile gas) are shown.

Total mobile CO_2 is the CO_2 that has not been trapped by dissolution, residual trapping, or mineral trapping. The mobile CO_2 is calculated from phase saturations in grid cells in which relative permeability of CO_2 phase is greater than zero. Total mobile CO_2 is expressed as percent of total CO_2 injected.

Maximum lateral distance is the distance the CO_2 plume (defined as region in which CO_2 phase saturation is nonzero) travels in the (sub-) horizontal or up-dip direction from the injector in 1000 years. The longer the distance the plume travels, the higher is its probability to intersect leaky faults or abandoned wells. Some plumes reach the edge of the simulation domain, and in these cases the lateral extent can be estimated by calculating the plume velocity in the up-dip direction and multiplying by 1000 years.

Time to reach the top seal is calculated as the time when any of the top layer grid blocks have non-zero CO_2 phase saturation. If CO_2 is injected across the entire thickness of the aquifer, time to reach top is zero. If CO_2 is injected in the lower regions of the aquifer, CO_2 will move vertically until it is either trapped or reaches the top seal. If CO_2 is still mobile, the plume will move laterally under the top seal.

Risk Parameters Correlated by Gravity Number

The catalog results are observed to be correlated to the Gravity number (N_{gv}), which is the dimensionless ratio of gravity forces to viscous forces in a reservoir. In general, the gravity number determines the shape of the CO_2 plume in an aquifer and is a convenient way to parameterize the CF catalog results. The various properties of the simulations carried out to generate the catalog can be grouped into the Gravity Number

$$N_{gv} = \frac{k_v \Delta\rho g \cos\alpha}{\mu u_{inj}} \qquad \text{Equation 1}$$

Here k_v is vertical permeability, $\Delta\rho$ is density difference between brine and CO_2 at aquifer temperature and pressure, α is the dip angle, μ is CO_2 viscosity, and u_{inj} is the injection velocity. The injection velocity is computed at the wellbore/formation interface by

$$u_{inj} = \frac{Q}{A_w} = \frac{Q}{2\pi r_w h_p} \qquad \text{Equation 2}$$

where Q is the volumetric injection rate, A_w is the circumferential area of the well, r_w is the well radius and h_p is the perforation interval.

Figure 4 shows an example simulation result of saturation profiles after 20 years for two different gravity numbers. The aquifer is 500 ft (150 m) thick and horizontal permeability is 100 md in both the cases. The gravity number is varied by changing injection rate and vertical permeability. In Case "a" the injection rate is 15 MMscfd (8.8 kg/s) and vertical permeability is 3 md, yielding N_{gv} = 0.013. In Case b the corresponding values are 10 MMscfd (5.9 kg/s), 10 md and 0.07. The higher gravity number case (Case b) has more gravity override of CO_2 and the CO_2 travels a longer distance beneath the top seal reaching 6000 ft (1800 m) in 20 years. In Case a the flux distribution along the perforated interval is almost uniform resulting in the plume contacting more rock and brine in the lateral direction and thus enhancing trapping. The gravity override is very small and the lateral distance traveled in 20 years is 2750 ft (840 m). As this example shows, higher gravity number is detrimental to CO_2 trapping efficiency. The ability to capture general trends such as this one is an advantage of using a catalog in the CF.

(a) (b)

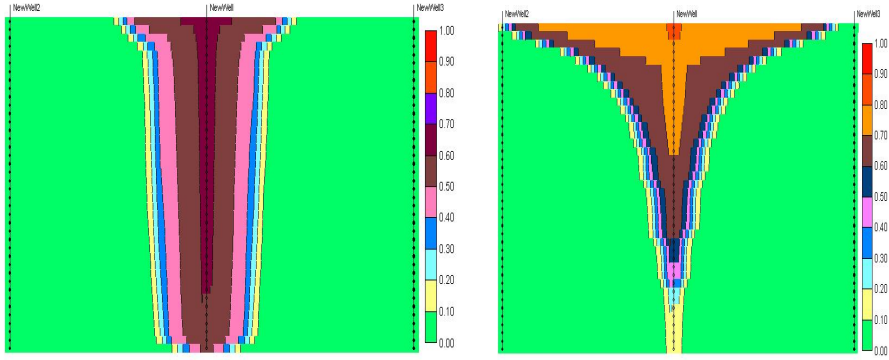

Figure 4. a) CO_2 plume for lower gravity number (N_{gv} = 0.013) after 20 years of injection. The plume moves almost uniformly away from the well in the lateral direction. b) CO_2 plume for higher gravity number (N_{gv} = 0.07) after 20 years of injection. There is preferential vertical movement of the plume and greater gravity override.

Example of Time to Hit Top Seal

To demonstrate the use of parameterizations derived from the catalog, we present an example of the time to hit the top seal. The data were extracted from the simulations carried out to generate the catalog. The correlation improves if time t to hit top seal is normalized by a characteristic time t^* given by

$$t^* = \frac{(H - h_1)h_2 r_w \phi}{Q} \qquad \text{Equation 3}$$

where H is the formation thickness, h_1 is the distance to the top perforation in the vertical well from the aquifer bottom, h_2 is the perforation interval, and ϕ is porosity. In short, t^* is the time for the plume to arrive at the top seal if it were traveling at constant velocity v corresponding to the radial velocity at the wellbore:

$$v = \frac{Q}{\phi A_w} = \frac{Q}{2\pi r_w h_2 \phi} \qquad \text{Equation 4}$$

For large gravity number, the plume travels almost vertically and t/t^* approaches unity. For small gravity number, the plume travels more in the lateral direction, and $t/t^* << 1$. Thus dimensionless time (t/t^*) is correlated inversely to gravity number.

For the simulations included in the catalog, the plot of dimensionless time to hit the top vs. gravity number, Figure 5, shows considerable scatter, but an inverse relationship is evident as expected

from the above discussion. The data points on the plot correspond to various simulations run with varying porosity, permeability, permeability anisotropy, thickness, depth, and perforated interval.

Higher gravity number generally has these effects:

- Preferential vertical movement and thus smaller time to hit the top.
- In a dipping aquifer, once the plume reaches the top seal it travels faster.
- Trapping is reduced as the plume does not come in contact with as much rock and brine in the direction transverse to plume movement.
- In large perforated sections, only a fraction of perforations contribute to injection.

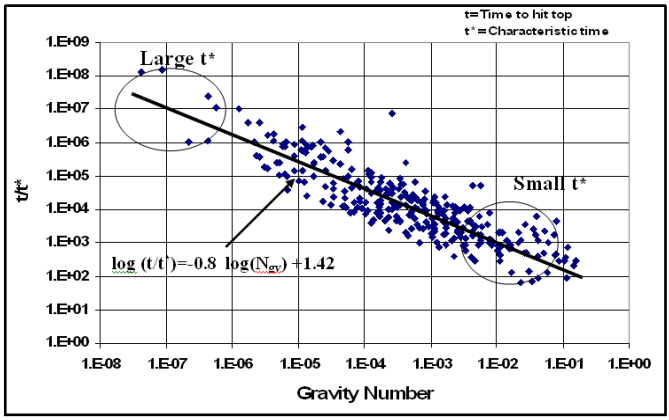

Figure 5. Plot of dimensionless time to hit top seal vs. gravity number. The data points are from simulations carried out by varying porosity, permeability, permeability anisotropy, thickness, depth, and perforated interval.

Using catalog for estimating risk parameters for actual aquifer

The simulation catalog includes cases for low, medium and high values of the shaded properties listed in Table 1. Most aquifers will not have all properties similar to any one case in the database. For a particular aquifer, we can estimate the risk parameters with simple correlations, or by interpolation from the closest database case. As an example of the former, the time to hit the top seal can be estimated by calculating the gravity number and characteristic time (t^*) for the target aquifer, then using the trend line in Figure 5. Examples of interpolation for lateral extent and fraction of mobile CO_2 are described in [9].

FAULT POPULATION STATISTICS

In order to calculate the likelihood of intersection of the CO_2 plume (or brine pressure perturbation) with conductive faults, we developed a method based on fault population statistics [10, 11]. These statistics can be measured from available fault coverages (geologic or structure maps) near or at a prospective site. Combining this information with an estimate of the anticipated plume size, shape, and orientation (obtained from the reservoir simulation catalog) allows calculation of the probability of the plume encountering a fault of a particular size.

Fault Population Statistics

Numerous investigators have found that fault length and displacement populations evolve with increasing strain, but typically follow a power-law distribution from low to moderate strains. This finding is based upon field research (e.g., [12]), physical modeling (e.g., [13]), and numerical simulations (e.g. [14]). Power-law distributions are of the form

$$N_d \propto d^{-C_d} \qquad \text{Equation 5}$$

where N_d is the number of faults with displacement greater than d, and C_d is the power law exponent.

Fault Density

Values of N_d are dependent upon the area of interest. The areal density of faults, F, is more useful as it is not dependent on area, which is based on CO_2 plume size in the current application. Values of F can be accurately calculated by measuring the length of faults with greater than a certain displacement in an area and dividing by the area. Structure contour maps are a typical source for such data. Because values of N_d are defined based on scan-line intersections and therefore contain length information, F can be substituted for N_d in Equation 5 [11] and follows the same pattern as of N_d. This substitution yields

$$F \propto d^{-C_d} \qquad \text{Equation 6}$$

and

$$\log F \propto -C_d \log d \qquad \text{Equation 7}$$

Equation 7 indicates a log-log plot of F against d will be linear if the fault population follows a power-law distribution. In addition, F approaches infinity as d approaches 0. This implies F becomes very large at the actual lower limit of d. This suggests a high probability that a given CO_2 plume will encounter a fault of some size. Of course, most such faults will have such small displacements as to not be of serious concern for leakage. This suggests that the concern for leakage should be on faults of a certain size (large enough to have a high probability of leakage) rather than on all faults encountered.

Fault Encounter Probability Estimation

The method used by the CF to calculate the probability of a CO_2 plume encountering a fault proceeds by the following steps.

1) Identify fault coverage(s) (fault-map data) relevant to a proposed site.
2) Measure fault lengths, orientations, and displacements from the coverage(s).
3) Define fault orientation modes through plotting and/or statistical analysis.
4) Calculate F at various d for each orientation mode.
5) Plot F versus d in log-log and semi-log space.

6) Model *F* distribution as power-law (or exponential, characteristic, or some combination if necessary) with consideration of resolution limit and possible sampling bias.
7) Use the modeled *F* distribution to define a distribution specific to the proposed site.
8) Calculate the encounter probability at the *d* of interest from site-specific *F*-distribution model, fault orientation modes, and CO_2 plume area, aspect ratio, and orientation estimated from reservoir simulation.

Fault Coverage(s), Measurements, and Calculations

Fault coverage(s) relevant to a proposed site can consist of oil or gas field structure maps, gas storage facility structure maps, or regional geologic maps. Measurement proceeds by fault segment, rather than by fault. To calculate *F* for a given *d*, the total length of the fault segments with displacement greater than *d* (displacement cutoff) must be calculated. Using the measured fault lengths, displacements, and areas, log-log plots are constructed of fault density versus displacement cutoff as shown in the example for the Kimberlina site in the southern San Joaquin Valley, California (Figure 6). Note this example uses throw truncation (vertical offset cutoff) instead of displacement cutoff because most of the faults are normal and near vertical, so the available structure maps show only throw, not displacement.

Selected data on Figure 6 are fit to a power-law distribution. The data appear exponential, with the data departing from a power-law fit at a throw cutoff of approximately 65 ft (20 m). This value is consistent with the resolution of the oil and gas field structure maps, however. The departure is due to the resolution limit inherent in mapping rather than reality. Consequently, the linear fit appears more likely to represent the actual fault population in the vicinity of the Kimberlina site, indicating that the fault population follows a power-law distribution. The power law fit also yields higher fault density estimates, which makes it more conservative than the exponential fit for estimating leakage risk. Adjusted data and associated power law are also shown on Figure 6 to account for the "finite-range" sampling effect [15].

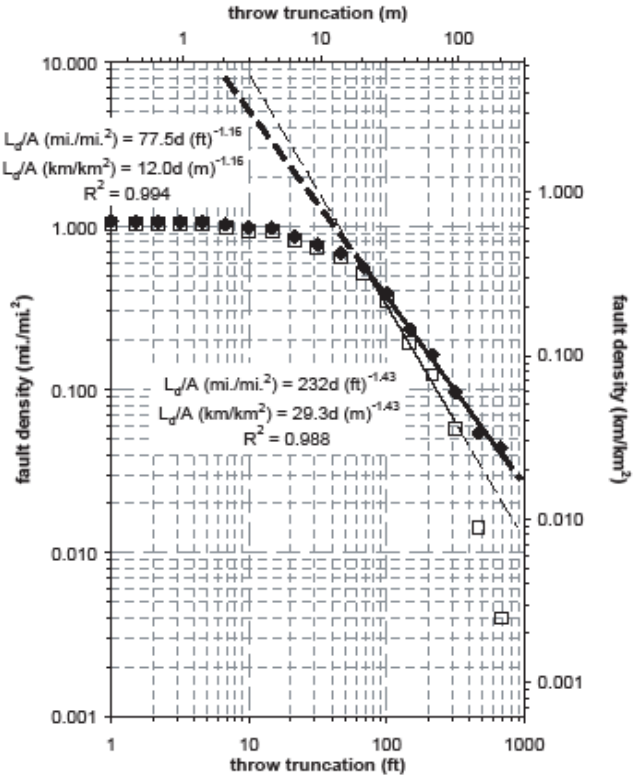

Figure 6. Measured data on throw truncation and fault density for the Kimberlina site in the southern San Joaquin Valley, California. Open boxes are raw data and filled boxes are data adjusted to account for the "finite-range effect."

Calculating Plume Fault Encounter Probability

Consider 100 randomly located plumes and a single randomly located fault of size L_f as shown in Figure 7. In this case, the probability of intersection, g, is given by

$$\Pr(g) = A_f \,/\, A_0 \qquad \text{Equation 8}$$

where A_0 is the area of interest and A_f is the area of the fault. This approach assumes that the fault or faults cross the entire area of interest (A_0), and that each plume only encounters one fault. The first condition is equivalent to assuming that faults are large relative to A_0, and the second condition is equivalent to assuming the spacing between faults is large relative to the plume diameter. As the spacing between large faults is generally greater than between small faults, these assumptions are

qualitatively in agreement. With these assumptions, if a plume is centered within a distance equal to the plume radius, *r*, the plume will intersect the fault (an event represented by *g*). Given that the fault has two sides

$$A_f = 2rL_f \qquad \text{Equation 9}$$

where L_f is the length of fault in the study area (shown as L on Figure 6). L_f can also be written as the areal fault density F times A_0:

$$L_f = FA_0 \qquad \text{Equation 10}$$

Substituting Equation 10 into 9, 9 into 8, and canceling terms gives

$$\Pr(g) = 2rF \qquad \text{Equation 11}$$

The value of F is measured from fault maps (as discussed), and the value of r can be approximated by numerical simulation. If the plume margin is some shape other than circular, then Equation 8 can be generalized to any plume shape by substituting half the plume dimension perpendicular to the fault, s:

$$\Pr(g) = 2sF \qquad \text{Equation 12}$$

The value of s can be measured directly from plots of the area swept by mobile CO_2 as modeled by numerical simulation.

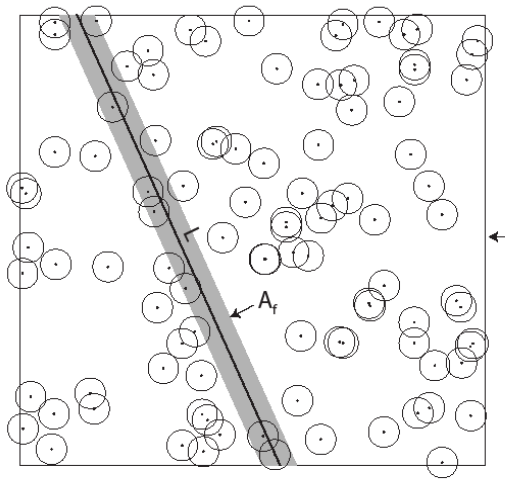

Figure 7. Diagram of 100 randomly located, circular plumes and a randomly located fault. Any plume geometrically centered within the shaded area will encounter the fault.

If the relationship between F and d is power law, then

$$\Pr(g) = 2sBd^{-C_d} \qquad \text{Equation 13}$$

where B is a proportionality constant. For elliptical plumes, the plume dimension perpendicular to the fault (s) can be calculated from the plume area, aspect ratio (eccentricity), and the acute angle between the long axis of the plume and the fault orientation of interest [11]. As mentioned, this approach assumes the fault-perpendicular plume dimension is considerably less than the distance between faults (fault spacing). As the plume dimension approaches the fault spacing, this approach will overestimate Pr(g) because the chance a plume will encounter two faults will be non-negligible. Consequently, this approach is more prone to false positives than false negatives for risk mitigation.

Numerical simulation indicates the CO_2 plume at the Kimberlina Pilot site in the San Joaquin Valley, California, will be elliptical due to the dipping reservoir. The sealing formation over the storage target at the site has a vertical thickness of approximately 180 m (590 ft). A throw truncation equal to the seal thickness is one threshold of concern (although such a fault may not be a leakage conduit due to its reservoir properties). The adjusted fault density equation on Figure 6 indicates the average fault density, F, at this throw truncation is 0.028 km/km^2 (0.046 mi./mi.^{2}). This is a low density, so the condition that the fault-perpendicular plume dimension is much smaller than the spacing between faults is sufficiently met to use the probability estimation of Equation 12. The distribution of Pr(g) at this fault density and simulated plume area, but varying plume aspect ratios and orientations, is shown on Figure 8. The simulated plume has an aspect ratio of 1.32 and a plume axis to predominant fault angle of 70°. Given these values, the Kimberlina plume Pr(g) for a fully seal-offsetting fault is 3.3%.

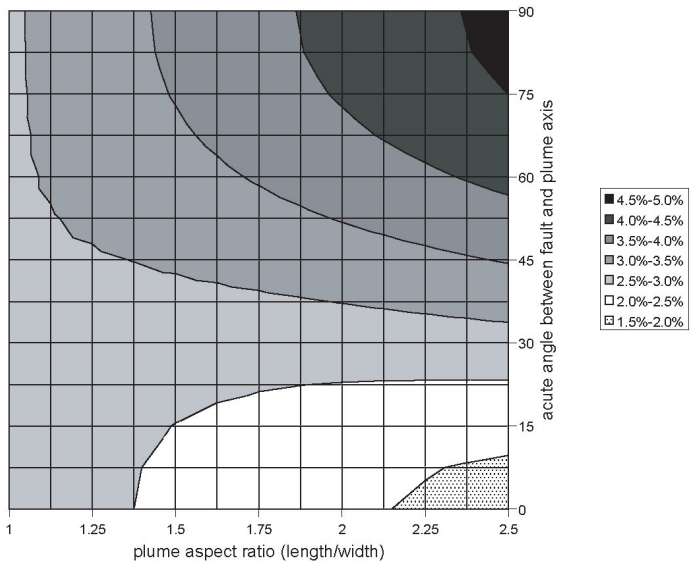

Figure 8. Probability the Kimberlina plume will encounter a fault fully-offsetting the seal as a function of the plume aspect ratio and the angle between the plume axis and the fault.

Summary

The probability of CO_2 leakage via a fault is the product of the probability a plume will encounter a fault and the probability of flow occurring along the fault through the seal. As described, the former probability can readily be calculated. The latter probability is dependent on the reservoir properties of the fault zone with respect to CO_2 flow (permeability, relative permeability, porosity, residual saturation, capillary entry pressure, etc.). The probability distribution of these properties are currently poorly constrained, and are a critical research area for GCS, as well as oil and gas exploration and production, nuclear waste repository selection and design, and groundwater hydrology.

PROBABILITY OF FAULT CONNECTIVITY

The objective of the fault connectivity model component is to provide a methodology for calculating P_{leak}, the probability that a CO_2 plume will encounter a system of conduits that is connected to a compartment that may be impacted by leakage and cause potential health, safety and environmental issues [16, 17]. The fundamental problem addressed by the approach is presented graphically in Figure 9. The fault population statistics approach described above allows estimation of the likelihood of a CO_2 plume encountering a fault large enough to be a leakage conduit. However, it does not address the question of the likelihood of that conduit connecting to a compartment much higher in the stratigraphic column, e.g., to USDW. Nor does it account for the likelihood of that conduit connecting to another conduit, e.g., another conductive fault. To address this issue, analysis of the likelihood of existence of a fault network must be considered as discussed in this section.

The probability that the CO_2 plume leaks into a compartment through faults or fractures is related to (1) the geometric characteristics of the system of conduits (i.e., distribution and connectivity of faults and fractures) between the storage reservoir and the compartment, and (2) the size and location of the CO_2 plume. For a site (which includes the storage formation and the geological formation above it) to be selected for GCS, some fault and fracture distribution data are expected to be available. However, the information on the conduit system is usually limited and highly uncertain. Moreover, the location and size of the CO_2 plume are also highly uncertain given the uncertain properties of the deep storage reservoir. Therefore, it is a challenge to predict (1) whether the conduits are connected, and if so, (2) the probability that a CO_2 plume will encounter the connected pathways.

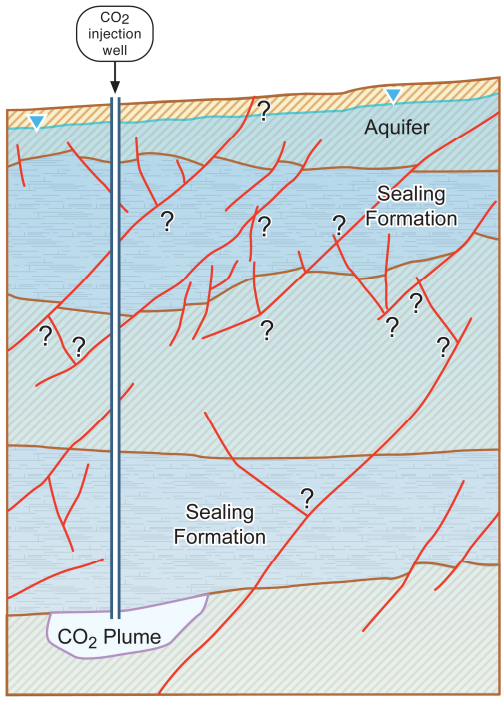

Figure 9. Schematic geologic cross section (not to scale) showing CO_2 injection well, CO_2 plume, reservoir, sealing formation, overlying formations, and potable ground water, along with conductive faults that may or may not intersect as indicated by the question marks.

Methodology

The proposed approach includes four steps: (1) estimate a critical value (α_c) for the parameter α, which is related to the density of conduits (faults and fractures), such that when this critical value is reached, the system is on average connected between the storage formation and a compartment; (2) estimate the probability that the CO_2 plume will encounter the connected conduits for a system with $\alpha \geq \alpha_c$, for various distributions of conduits, system sizes and CO_2 plume sizes; (3) construct fuzzy rules that relate information about the conduit system and CO_2 plume size to leakage probability; and (4) for given system characteristics, predict the probability that a CO_2 plume will escape from the storage formation to a compartment through connected conduits.

We make the following assumptions:

- The system under investigation is a square, two-dimensional (2D) cross section with sides of length L.
- Faults/fractures are randomly oriented.
- Faults/fractures considered are conductive.
- Faults/fractures follow a power-law length distribution.

The third assumption means this method provides an upper bound estimate of leakage probability. The method assumes if a "conductive" pathway exists, leakage along the pathway will occur, which discounts flow dynamics. For instance, flow may not reach the compartment given the limited duration of any actual injection and/or matrix permeability along the pathway.

Estimation of Critical Value α_c

Among different models for describing fault length distributions, the power-law distribution is the most widely used [18, 19, 20]:

$$n(l, L) = \alpha(L) l^{-a} \qquad \text{Equation 14}$$

where $n(l, L)dl$ is the number of faults having a length in the range $[l, l+dl]$, $\alpha(L)$ is a coefficient of proportionality that reflects fault density and depends on the system size L (assuming a square system with sides of length L), and a is an exponent, which typically varies between 1 and 3. It is apparent from Equation 14 that the power-law distribution contains no characteristic length. This is the key argument for using power laws to describe fault growth processes [21].

Percolation theory [22] has been applied to study the connectivity of fault systems. In percolation theory, a parameter p is used as an average measure of the geometric properties, generally related to the density of elements, which also provides information on the connectivity of the system. The percolation threshold p_c is defined as the critical p value below which (on average) the fault system is not connected, while when p is above the critical value p_c, the system is connected. In other words, 50% of the systems at the percolation threshold are connected. Bour and Davy [22] presented an analytical expression for the percolation threshold for a fault system following a power-law length distribution as:

$$p_c(L) = \int_{l_{\min}}^{L} \frac{\alpha_c(L) l^{-a} l^2}{L^2} dl + \int_{L}^{l_{\max}} \alpha_c(L) l^{-a} dl \qquad \text{Equation 15}$$

If $l_{max} < L$, the second term on the right-hand side drops out and the first term integrates to l_{max} instead of L.

Bour and Davy [22] also demonstrated that the percolation threshold $p_c(L)$ does not present significant variations with L. For a power-law fault length distribution with any value of a, the computed values of $p_c(L)$ are around 5.6 in two dimensions. By setting p_c to 5.6, an expression for the critical fault density $\alpha_c(L)$ can be obtained. Equation 15 can be normalized with respect to l_{min}, where $\alpha_{cs}(L_s) = \alpha_c(L) l_{\min}^{-a+1}$. The subscript s indicates normalized values with respect to smallest fault size l_{min}.

For a given system, we can calculate the critical parameter $\alpha_{cs}(L_s)$ and compare it to the actual parameter $\alpha_s(L_s)$. If the actual density is much smaller than the critical value, we can conclude that the system is not connected and the CO_2 plume will not be able to leak out through the fault system.

Generation of Conduit Network

To estimate the probability that a CO_2 plume escapes through the connected conduits and reaches compartments for a system with $\alpha(L) > \alpha_c(L)$, we vary system parameters to generate discrete fracture networks and perform Monte Carlo simulations. Three types of uncertainty are considered. The first results from our lack of knowledge of the system properties. This uncertainty is considered by using fuzzy-rule-based modeling to propagate the uncertainty of the input parameters in estimating P_{leak}. The second is the uncertainty in the generation of the discrete fracture network itself. Even for systems with the same parameters (e.g., system size and fracture distribution), the generated network could have very different connectivities. This uncertainty is considered by conducting Monte Carlo simulations. The third uncertainty is in the size and location of the CO_2 plume. In the simulation, we will vary CO_2 plume size and use a moving average to consider the uncertain location of the plume.

The parameters varied in the fracture network generation and P_{leak} calculations are the normalized system size L_s, the normalized maximum fracture length $l_{max\ s}$, the exponent a, the ratio of $\alpha_s(L_s)/\alpha_{cs}(L_s)$, and the normalized plume size M_s.

For each of the realizations of the generated network, the outcome has the following format:

IF $L_s = L_1$, $l_{max\ s} = l_1$, $a = a_1$, $r = \alpha_s(L_s)/\alpha_{cs}(L_s) = r_1$, and $M_s = M_1$
THEN the probability that a CO_2 plume escapes from the storage reservoir through a connected network of conduit (P_{leak}) is b.

where L_1, l_1, a_1, r_1 ($r_1 \geq 1$), and M_1 are the numerical values of the varying parameters in the simulation (crisp numbers) which should cover all possible values considered.

Construction of Fuzzy Rules for Calculating P_{leak}

Fuzzy set theory, introduced by Zadeh [23], has been used to deal with approximate (rather than exact) reasoning. In a fuzzy statement, A_i is a fuzzy number that reflects vagueness. Membership functions of a fuzzy number can have different shapes. Typically, triangular, trapezoid, or Gaussian memberships are used. Fuzzy rules can be used to model systems with imprecise or uncertain information. These rules can be developed using expert opinions, existing data, and qualitative information. Alternatively, fuzzy rules can be generated through numerical simulations. In our case, we use results from the fault network generation as a training set to construct fuzzy rules of connectivity.

An example of a fuzzy-rule statement using triangular membership functions is as follows (the numbers in this statement are dimensionless numbers that are normalized with respect the smallest fracture size):

IF a = (1.1, 1.5, 2.0) AND L_s = (50, 100, 200) AND l_{maxs} = (50, 100, 200)
AND r = (0.75, 1.0, 1.25) AND r_p = (0.2, 0.4, 0.6)
THEN P_{leak} = (0.01, 0.12, 0.18)

where $r_p = M_s/L_s$. Using the centroid method, the final defuzzified P_{leak} for this rule (when it is fulfilled) is 0.1.

Calculation of P_{leak} for a Given System

For a given system, the first step is to calculate $\alpha_{cs}(L_s)$ and compare it to $\alpha_s(L_s)$. If the latter is smaller, $P_{leak} = 0$. Otherwise, the above fuzzy rules are used to infer P_{leak}. To aggregate fuzzy rules, one option is to use the normalized sum combination method proposed by Bardossy and Duckstein [24]. Another option is to use the Mamdani-type inference system provided by the Matlab Toolbox, which uses a maximum combination method to aggregate fuzzy rules.

To demonstrate the approach, we use fuzzy rules to predict P_{leak} as a function of r_p (CO_2 plume size divided by system size) for a system with a of approximately 1.5, $l_{max\ s}$ of approximately 100, L_s of approximately 100, and a few values of $r = \alpha_s(L_s)/\alpha_{cs}(L_s)$. The final defuzzified P_{leak} are shown in Figure 10. Details of the method are presented in Zhang et al. [17].

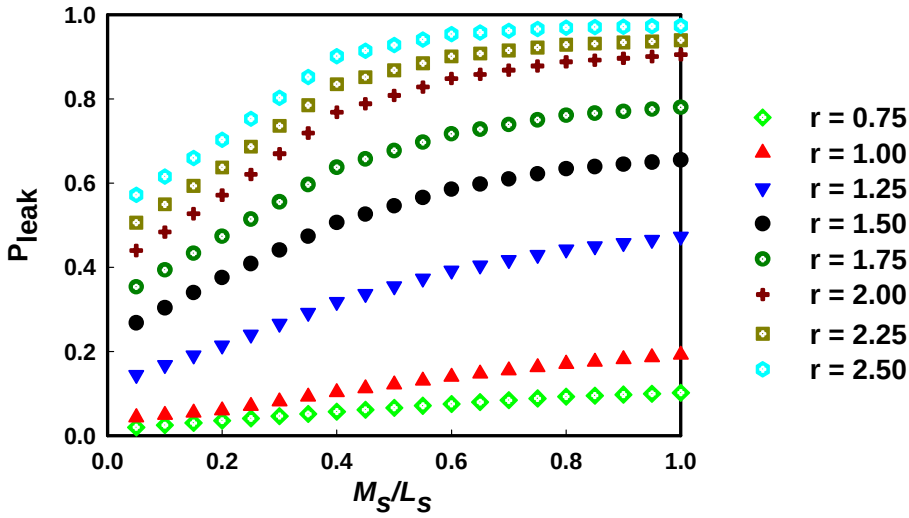

Figure 10. Fuzzy-rule based prediction of P_{leak} as a function of normalized CO_2 plume size for a system with $a = 1.5$, $l_{max\ s} = 100$, $L_s = 100$, and different values of $r = \alpha_s(L_s)/\alpha_{cs}(L_s)$.

Summary

This fuzzy rule-based model component of the CF is used to estimate the probability (P_{leak}) of the plume intersecting a connected network of faults or fractures that also intersects a compartment in which impact may occur. The main computational effort of the approach lies in the numerical generation of the fracture networks. However, this only needs to be done once to provide the basis for constructing the fuzzy rules; predictive simulations are then performed very efficiently using these fuzzy rules. The uncertainty of P_{leak} is predicted by propagating the uncertainty in the input parameters. The method can be extended to apply to brine leakage risk by using the size of the pressure perturbation above some cut-off value as the effective plume size. The method can also be extended to account for non-random fault/fracture orientations, stratigraphic connections between faults/fractures, and three rather than two spatial dimensions.

WELLBORE FLOW

The wellbore flow model component is used in the CF to model leakage up wells [25]. The focus of this work in on the upward (or downward) flow in the well occurring either in the tubing, within an annular region between casings, or between the casing and the rock, all of which fall into non-Darcy flow regimes. Regardless of the region in which flow is occurring, physical processes involving viscous or turbulent flow, phase change, and advective and diffusive mass and heat transfer are relevant. In this work, we focus on two-phase flow of CO_2 and brine with non-isothermal effects and neglect well cement degradation and geomechanics.

Methodology and Verification

The approach we use for describing wellbore flow is based on the drift-flux model (DFM) [26] for transient two-phase non-isothermal flow of CO_2-water mixtures. Conservation equations for mass, momentum, and energy under different flow regimes in the wellbore are solved numerically while wellbore heat transmission is handled semi-analytically. We implement the DFM in TOUGH2 [27] with the ECO2N equation of state module [28]. The conventional approach for calculating the mixture velocity in the DFM is often based on the steady-state pressure loss equation for wellbore flow [29]. To improve simulation performance in wellbore flow processes involving high fluxes, we have extended the DFM to include the transient terms of the momentum conservation equations in calculating the velocity from the pressure gradient.

To calculate the mixture velocity, we use the transient momentum conservation equation with the steady-state assumption about the wall shear stress

$$\frac{\partial}{\partial t}\left(\rho u_m\right)+\frac{\partial}{\partial L_w}\left(\rho u_m{}^2\right)=-\frac{\partial P}{\partial L_w}-\frac{f\,\rho u_m^2}{4r_w}-\rho g\cos\theta \qquad \text{Equation 16}$$

where u_m is the mixture velocity in the wellbore, L_w is a length of the wellbore section (positive upward), ρ is the mixture density, and θ is the local angle between wellbore section and the vertical direction. The friction coefficient (f) is a function of the Reynolds number (Re) for laminar and turbulent flows (Re = $\rho u_m d/\mu$ where μ is the mixture viscosity and d is the wellbore diameter) and is given by

$$f=\frac{64}{\mathrm{Re}}\ \text{for Re} < 2400, \text{ and } \frac{1}{\sqrt{f}}=-2\log\left[\frac{2\varepsilon/d}{3.7}-\frac{5.02}{\mathrm{Re}}\log\left(\frac{2\varepsilon/d}{3.7}+\frac{13}{\mathrm{Re}}\right)\right]$$

for Re > 2400 Equation 17

[29]. When the system reaches steady state there is no mass accumulation, and Equation 16 reduces to the pressure loss equation [30] given by

$$-\frac{dP}{dL_w}=\frac{f\,\rho\,u_m^2}{4r_w}+\rho\,u\frac{du_m}{dL_w}+\rho\,g\cos\theta \qquad \text{Equation 18}$$

To verify the wellbore flow solution approach, we simulated a case of steady-state single-phase water flowing up the wellbore at 25 ^{o}C at a rate of approximately 2 kg/s and compared the result with the theoretical pressure profile along the well as calculated from the steady-state pressure loss equation. A sketch of the model system used for this verification problem and for the test problem that follows is shown in Figure 11a. The initial conditions are hydrostatic pressure, temperature varying linearly from 15-45 ^{o}C, and 100% water in the well. In the verification problem, we set a higher pressure at the bottom boundary and ran the model to steady state (at ~2 kg/s) under isothermal conditions (25 ^{o}C). Shown in Figure 11b are the theoretical and calculated pressures along the wellbore, along with the relative error showing a very close match. This verification problem confirms the ability of the code to solve a steady-state single-phase flow up the well.

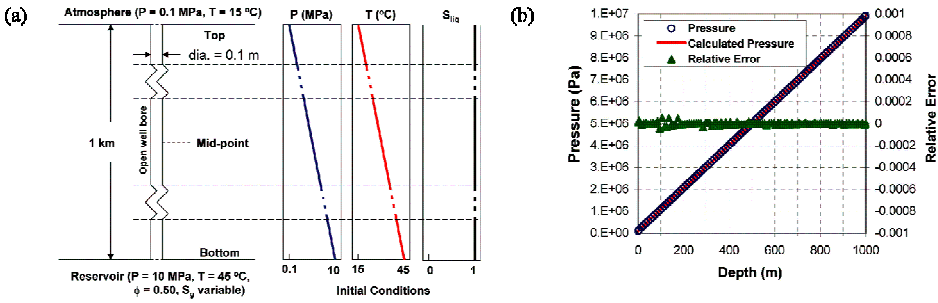

Figure 11. (a) wellbore boundary and initial conditions. (b) steady-state pressure and relative error in flowing well for verification.

Example Results

We present here results for a case of two-phase flow up an open wellbore. The scenario envisioned is that of the encounter of the edge of a migrating CO_2 plume at 10% phase saturation encountering an open well initially filled with water. The focus is on flow in the wellbore, and we assume residual gas saturation in the reservoir is 0.05. Starting from hydrostatic conditions, an overpressure of 0.1 MPa (1 bar) is applied to the reservoir.

With reference to Figure 12, we observe in this test problem the early-time upward flow within the well of water at all depths as driven by the 0.1 MPa pressure perturbation at the bottom. Gas flow does not begin until approximately t = 20 s when gas is present at the bottom. By t = ~500 s, gas flows at the middle and top of the well. The flow rate of CO_2 reaches approximately 1.4 kg/s in this open wellbore case and the final Reynolds numbers are between 5.1 x 10^5 (at bottom) and 4.7 x 10^6 (at top).

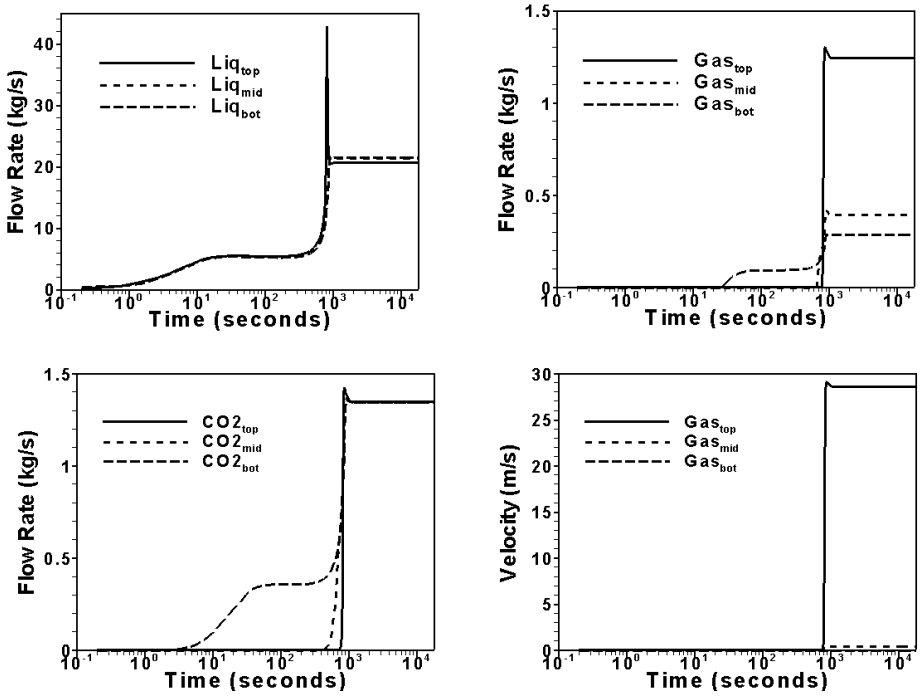

Figure 12. Flow rates and velocities of CO_2 and water at three levels in the well (bottom, middle, and top).

Further insight into the processes modeled can be obtained from Figure 13 which shows gas saturation, gas density, pressure, and temperature throughout the well as a function of time. As shown, the well is initially filled with water and gas progressively fills the well from the bottom up. After 30 minutes (1800 s), gas is fairly evenly distributed throughout the well from 10% at the bottom to nearly all gas at the top. The reasons for this increase in gas saturation are (1) the exsolution of gas from the liquid as pressure drops and (2) the large expansion that CO_2 undergoes as it transitions from supercritical to gaseous conditions. This transition occurs around the critical pressure of 7.4 MPa (74 bar), at a depth of approximately 800 m. The gas density plot in Figure 13 shows the sharp decrease in gas density at depths around 800 m. Temperature also affects CO_2 solubility, but temperature becomes relatively constant as steady flow develops, resulting in decreasing CO_2 mass fractions being controlled mostly by pressure. The temperature contour shows the evolution from a conductive profile controlled by the geothermal gradient to an advective profile controlled by upward fluid flow. In between the initial and steady states, there are some local maxima and minima arising from expansion and dissolution of CO_2 as gas phase rises upwards.

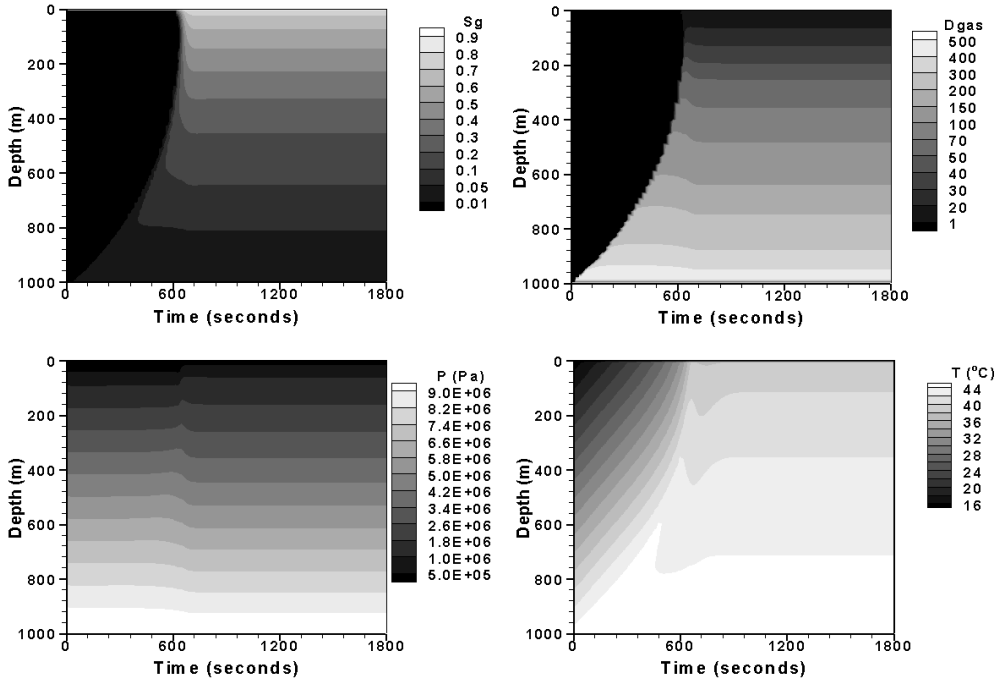

Figure 13. Profiles of gas saturation, gas density, pressure, and temperature in the wellbore as a function of time.

Summary

We have developed a wellbore flow simulator that models two-phase CO_2-brine mixtures for use in GCS leakage and injection studies [25]. This simulation capability was developed for quantifying potential leakage up wells using pressures and gas saturations at depth of CO_2 migration and pressure propagation that are calculated by reservoir simulation. Although the test problem is based on flow up an open borehole, the approach can be used for flow in an annulus region by suitable modifications of roughness coefficients and geometric parameters. The fundamental elements of advection, diffusion, and phase change are independent of the particular flow geometry. Similarly, the approach can be applied to leakage in non-vertical and horizontal wells with the caveat that flow in the well is always 1-D.

DENSE GAS DISPERSION

Dense gas dispersion capabilities were developed for the CF by modification of an existing numerical weather simulation model [31]. This component of the CF is intended to allow quantification of CO_2 concentrations in the NSE compartment. Because atmospheric dispersion of CO_2 is driven by gravity (gas-density contrast) and wind, the danger from CO_2 is greatest in regions with topographic depressions where the dense gas can pool, or under stably-stratified background atmospheric conditions which further inhibit mixing and dilution of the gas.

We have used the new capability to demonstrate the ability of common topographic depressions to trap accumulated CO_2 for extended periods and at concentrations that exceed limits allowable for

continuous or instantaneous exposure; accumulated CO_2 can persist for shorter periods even under high ambient winds. A variety of simulations of different release strengths and background atmospheric conditions allows the generation of a catalog of results analogous to the reservoir simulation catalog that can be queried to identify hazardous scenarios.

Approach

We extended a mesoscale atmospheric model (Advanced Regional Prediction System (ARPS)) to predict dispersion of releases of dense CO_2 gas. ARPS allows specification of complex terrain, land-surface fluxes, heterogeneous land cover, time-dependent weather forcing, etc. and can be run as a large-eddy simulation (LES) code that solves the three-dimensional, compressible, non-hydrostatic, filtered Navier-Stokes equations. ARPS is described in detail by Xue et al. [32, 33].

ARPS was modified to include a scalar-advection diffusion equation for dense gas transport described by the equation

$$\frac{\partial \rho X_c}{\partial t} + u\frac{\partial \rho X_c}{\partial x} + v\frac{\partial \rho X_c}{\partial y} + w\frac{\partial \rho X_c}{\partial z} = \frac{\partial}{\partial x}\left(\kappa_T \frac{\partial \rho X_c}{\partial x}\right) + \frac{\partial}{\partial y}\left(\kappa_T \frac{\partial \rho X_c}{\partial y}\right) + \frac{\partial}{\partial z}\left(\kappa_T \frac{\partial \rho X_c}{\partial z}\right)$$

Equation 19

where X_c is the mass fraction of the gas in a particular cell, u, v, and w are the velocity components in the x, y, and z directions, respectively, κ_T is the turbulent eddy diffusivity, and ρ is the total density in kg/m^3. Note that the entire quantity ρX_c is solved for at each time step (i.e., the two quantities are not calculated separately). Active scalar (i.e., dense gas) transport required modifying two areas of the model: (1) calculation of density, and (2) calculation of buoyant forcing in the w-equation. This allows incorporation of the total density (due to air and the dense gas) into the buoyancy forcing, which appears in the vertical momentum equation. The density field thus couples the equation describing transport and dispersion of the dense gas with the momentum equations, causing the model to feel the effects of density-driven flow. Note that the ARPS system of governing equations does not allow for large mass fluxes across a boundary, hence the current formulation can accommodate instantaneous releases only.

Passive vs. Dense Gas Dispersion

The behavior of dense gases such as CO_2 can be quite different from that for passive tracers (with neutral buoyancy) due to density effects [34]. For example, a plume of CO_2 will spread laterally over flat terrain even in the absence of wind because it is denser than the surrounding air. Driven by density effects, a CO_2 plume will spread more quickly than a neutrally-buoyant gas which spreads only through diffusion, giving the counter-intuitive result that ground-level concentrations can drop more quickly for a dense gas than for a passive gas tracer under calm conditions. The hazard of prolonged exposure to CO_2 at high concentrations, however, lies in the fact that topographical depressions or basins provide preferential sites for accumulation and immobilization. The presence of negatively buoyant gas in sufficient amounts can prevent the scouring of the gas from a basin by ambient winds.

The impact of topography and ambient conditions on scalar dispersion can be illustrated through examination of a two-dimensional idealized basin described by mirror sigmoid functions. Simulations using the new capability were performed on a computational domain of 200 x 60 grid cells, with Δx = 5 m and a stretched grid in the vertical with a minimum resolution of Δz = 0.25 m

and an average resolution of 2 m. The top and bottom boundaries are rigid, and there is a Rayleigh damping layer beginning at z = 80 m. An instantaneously released mass of CO_2 is initialized at the bottom of a depression. A logarithmic wind profile is initialized across the domain and held constant as an inflow condition on the left, as shown in Figure 14. The passive scalar is quickly transported out of the basin (solid lines), while the CO_2 plume (gray contours) lingers in the basin even under strong winds (~5 m/s).

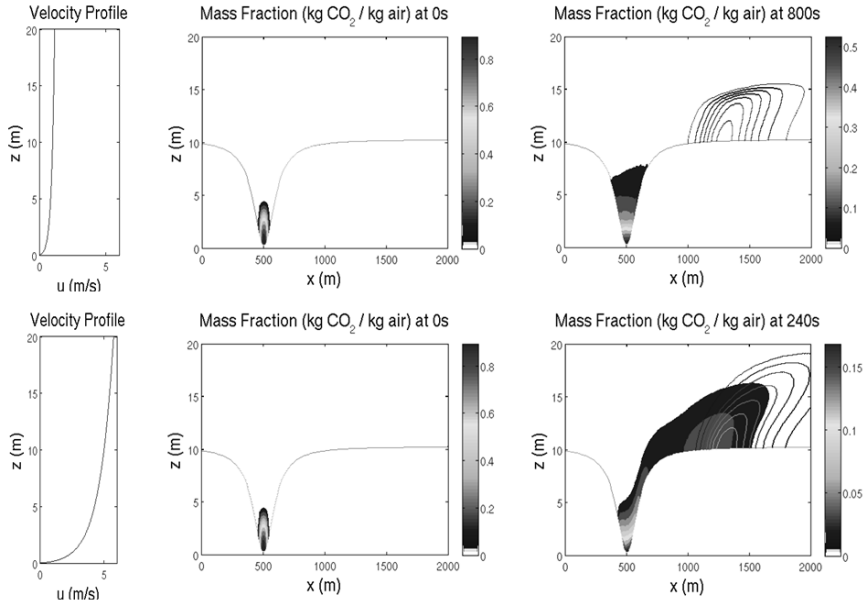

Figure 14. Scouring from a 2D trench. Shaded contours show mass fraction of CO_2 (CO_2 mass fraction is highest at the deepest part of the trench) and solid lines show passive tracer. Profiles on left indicate driving wind at left edge of domain.

CO_2 Atmospheric Dispersion Catalog

A catalog of CO_2 dispersion and accumulation scenarios, analogous to the reservoir simulation catalog, was created for different topographies, release scenarios, and meteorological conditions.

Four types of terrain were used in the simulation scenarios: (A) completely flat ground, (B) flat ground interrupted by a long trench of depth 10 m, (C) flat ground interrupted by a step change in elevation (shelf) of 10 m (a half-trench), and (D) a set of rolling hills of maximum amplitude 50 m (see Figure 15). The domain size is (203, 143, 43) grid points in the x, y, and z directions, respectively, for all cases except the rolling terrain where it is (163, 203, 43). The simulations all use the same grid spacing ($\Delta x = \Delta y$ = 5 m, Δz_{avg} = 2.5 m, Δz_{min} = 0.25 m near the ground, stretched above) and time steps (Δt = 0.02 s, $\Delta \tau$ = 0.002 s). Lateral boundary conditions are zero-gradient. Top and bottom boundaries are rigid walls, with a log-law condition specified at the bottom

boundary to account for surface drag (as is typical in all mesoscale prediction models). A Rayleigh damping layer is used at the top of the domain above 80 m. All simulations use a 1.5 order turbulent kinetic energy formulation for the large-eddy simulation turbulence closure.

Wind speeds were chosen from the following set: 0 m/s (calm conditions), 0.5 m/s, 1 m/s, 2 m/s, and 4 m/s. Winds were initialized uniformly over the domain. Shear develops at the ground after the simulation is started due to drag at the surface (corresponding to an effective roughness height of 0.1 m). A range of wind directions can be selected but winds from the west were applied in the cases shown here. Neutral stratification and weakly stable conditions (with a vertical potential temperature gradient of approximately 0.01 K/m) were chosen. Releases are considered to be instantaneous, with a magnitude of either 1,000 kg (1 tonne) or 10,000 kg (10 tonnes) of CO_2 at the surface. A uniform hemispherical instantaneous release is specified, with a radius of 15 m in *x* and *y* and 6 m in *z* for the 1,000 kg release, or 30 m in *x* and *y* and 14 m in *z* for the 10,000 kg release.

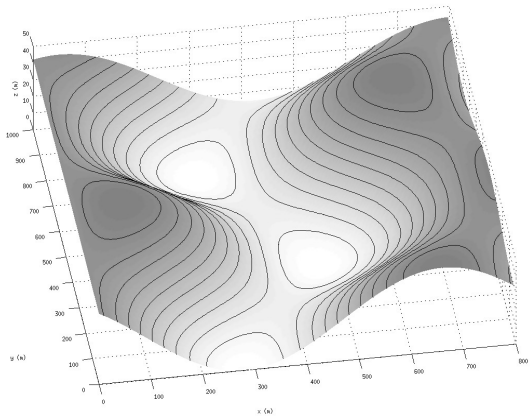

Figure 15. Rolling terrain used for catalog of ideal simulations.

For each case scenario, a number of parameters are extracted for analysis of plume extent and dilution time. Three concentration threshold levels are chosen which correspond to a Short-Term Exposure Level (STEL) for 15 minutes. The thresholds are based on mass fractions (i.e. kg CO_2/kg air) of 0.01, 0.03, and 0.1, which correspond to concentrations of 10,000 ppm (1%), 30,000 ppm (3%), and 100,000 ppm (10%). Severe headaches, diffuse sweating, and labored breathing begin at 30,000 ppm. The OSHA (U.S. Occupational Safety and Health Administration) occupational exposure standards are 0.5% CO_2 for a 40-hour work week average and 3% for a 15-minute exposure. The maximum instantaneous limit is 4%. All three exposure standards must be satisfied [5]. In addition to plume extent, local exposure times (in seconds) are provided for each of the chosen thresholds. Thus, if the overall exposure time is greater than 900 s (15 min) for the 0.03 mass fraction threshold, the STEL will have been exceeded. A series of three figures showing ground level concentration at 300 s, 600 s, and 900 s is provided for each simulation. A second series of three figures shows the amount of time spent above the three threshold concentrations as a function of *x*,*y* location, indicating which portion of the domain is at risk for exceeding the STEL.

Two examples of catalog results are given in Figures 16 and 17 for the rolling hills: Case D1 with no ambient winds, and Case D1 with a 1 m/s westerly wind. Both are initialized with a 10 tonne release of CO_2. The source location is marked with an 'x'. With no winds, the CO_2 flows downhill and collects in the valley. With a 1 m/s wind, the primary direction of plume spreading is still down-gradient (perpendicular to the mean wind direction), with significant accumulation in the valley. A portion of the plume even travels upwind of the source location. A large area in the valley exceeds the 0.01 threshold, and a smaller area exceeds the 0.03 concentration threshold for more than 15 minutes. Note that the threshold contours and statistics are calculated based on data at 60 s intervals.

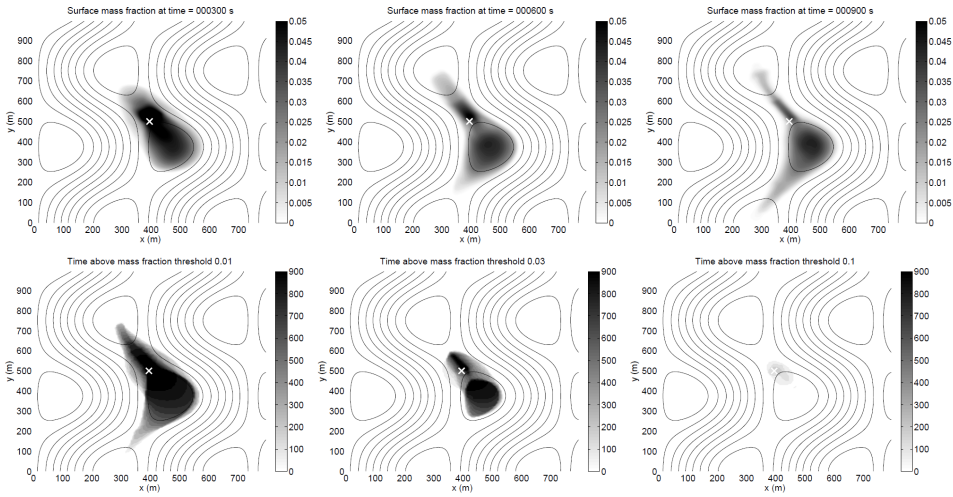

Figure 16. Case D1. Rolling hills with no winds, 10,000 kg release (marked by 'x'). Top panel shows surface CO_2 mass fraction contours. Bottom panels show exposure time above each threshold level (in seconds). Black lines show terrain contours.

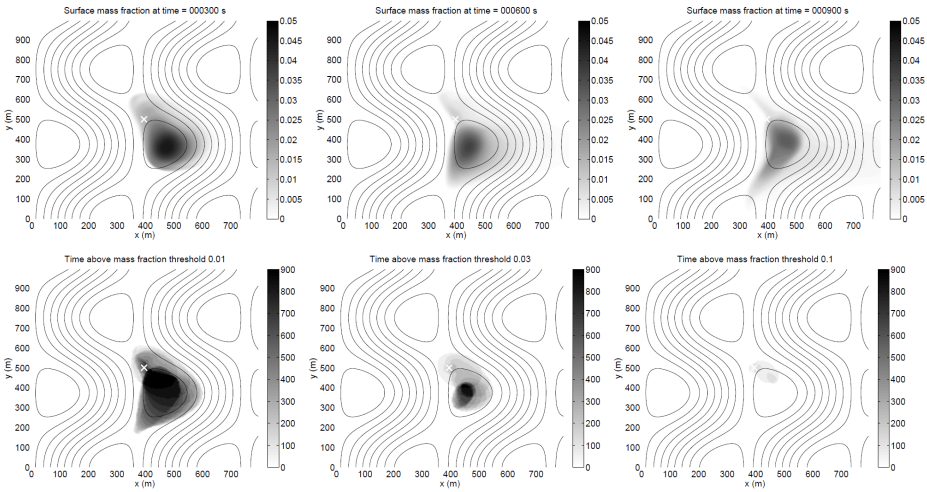

Figure 17. Case D2. As in Figure 16 but for 1 m/s background winds.

Summary

The model component on atmospheric dispersion in the CF allowed the generation of a catalog of idealized simulation results to demonstrate features of dense gas dispersion and to create a tool to allow stakeholders to carry out risk assessment for a particular CO_2 storage site by querying a database. A set of 22 simulations was performed to investigate the parameter spaces described above, including topography type, wind speed, stability, and release strength. It was found that topographic depressions of only 10-50 m in depth can lead to accumulation of CO_2 at hazardous exposure levels. Future work will be directed at adding a flux-type boundary condition capability to ARPS to handle incipient CO_2 leakage.

CONCLUSIONS

Although the CF invokes major simplifications of an actual GCS system, it requires sophisticated model components to carry out the analysis. We have presented above brief summaries of the five significant model components we have developed for the CF. Further details of the methods can be found in the references. Although the approaches described here are anticipated to be effective in many cases, undoubtedly applications of the CF to additional sites will reveal shortcomings and more effort in developing model components and/or underlying assumptions will be needed as the number and scale of GCS projects increase.

ACKNOWLEDGMENTS

We thank H.H. Liu (LBNL) for internal review, and Scott Imbus (Chevron) for support and encouragement. This work was supported in part by the CO_2 Capture Project (CCP) of the Joint Industry Program (JIP), and by Lawrence Berkeley National Laboratory under U.S. Department of Energy Contract No. DE-AC02-05CH11231.

REFERENCES

1. C.M. Oldenburg, S.L. Bryant, Certification Framework for Geologic CO_2 Storage, Sixth Annual Conference on Carbon Capture and Sequestration, National Energy Technology Laboratory, Pittsburgh, PA, May 7-10, 2007.
2. C.M. Oldenburg, J.-P. Nicot, S.L. Bryant, Case studies of the application of the Certification Framework to two geologic carbon sequestration sites, *Energy Procedia*, GHGT9 conference, Nov. 16-20, 2008, Washington DC. LBNL-1421E.
3. C. M. Oldenburg, S.L. Bryant, J.-P. Nicot, Certification Framework for Geologic Carbon Sequestration Based on Effective Trapping, *Int. J. of Greenhouse Gas Control*, in press, 2009.
4. R.P. Hepple, S.M. Benson, Geologic storage of carbon dioxide as a climate change mitigation strategy: performance requirements and the implications of surface seepage, *Environ. Geol.* **47**(4) (2005) 576.
5. Intergovernmental Program on Climate Change (IPCC) Special Report on carbon dioxide capture and storage, ISBN 92-969-119-4, http://www.ipcc.ch/activity/srccs/index.htm, 2005.
6. N. Kumar, CO_2 Sequestration: Understanding the plume dynamics and estimating risk, Univ. of Texas, Austin, Master's Thesis, 2008.
7. A. Kumar, R. Ozah, M. Noh, G.A. Pope, S. Bryant, K. Sepehrnoori, and L.W. Lake, Reservoir Simulation of CO_2 Storage in Deep Saline Aquifers, *Society of Petroleum Engineers Journal* **10**(3) (2005) 336.
8. L. Nghiem, P. Sammon, J. Grabenstetter, H. Ohkuma, Modeling CO_2 storage in aquifers with a fully-coupled geochemical EOS compositional simulator. Paper SPE 89474 presented at 2004 SPE/DOE Symposium on Improved Oil Recovery, Tulsa, Oklahoma, 17-21 April, 2004.
9. N. Kumar, S.L. Bryant, J.-P. Nicot, Simplified CO_2 plume dynamics for a Certification Framework for geologic sequestration projects, *Energy Procedia*, GHGT-9 conference, Nov. 16-20, 2008, Washington DC.
10. P.D. Jordan, C.M. Oldenburg, J.P. Nicot, 2008, Characterizing fault-plume intersection probability for geologic carbon sequestration risk assessment, *Energy Procedia*, Proceedings of GHGT-9, Washington, D.C., Nov. 17-20, 2009.
11. P.D. Jordan, C.M. Oldenburg, J.P. Nicot, Calculating the probability of injected carbon dioxide plumes encountering faults. In preparation.
12. J. Watterson, J.J. Walsh, P.A. Gillispie S. Eaton, Scaling systematics of fault sizes on a large-scale range fault map. *Journal of Structural Geology* **18**(2-3) (1996) 199.
13. R.V. Ackerman, R.W. Schlische M.O. Withjack, The geometric and statistical evolution of normal fault systems: an experimental study of the effects of mechanical layer thickness on scaling laws. *Journal of Structural Geology* **23**(11) (2001) 1803.
14. P.A. Cowie, D. Sornette, C. Vanneste, Multifractal scaling properties of a growing fault population. *Geophysical Journal International* **122**(1) (1995) 457.
15. G. Pickering, J.M. Bull, D.J. Anderson, Sampling power-law distributions, Tectonophysics No. 248 (1995) 1-20.
16. Y. Zhang, C.M. Oldenburg, P.D. Jordan, S. Finsterle, K. Zhang, Fuzzy Rule-Based Probability Estimation of Fault Leakage at Geologic Carbon Sequestration Sites, Energy Procedia, GHGT9 conference, Nov. 16-20, 2008, Washington DC. LBNL-1415E.
17. Y. Zhang, C.M. Oldenburg, S. Finsterle, Percolation-Theory and Fuzzy Rule-Based Probability Estimation of Fault Leakage at Geologic Carbon Sequestration Sites, *Environmental Geology*, in press.
18. G. Gudmundsson, Geometry, Formation and Development of Tectonic Fractures on the Reykjanes Peninsula, Southwest Iceland, *Tectonophysics* **139**(3-4) (1987) 295.
19. H. Scholz, P.A. Cowie, Determination of Total Strain from Faulting Using Slip Measurements, *Nature* **346**(1990), 837.

20. P. Segall, D.D. Pollard, Joint Formation in Granitic Rock of the Sierra-Nevada, *Geological Society of America Bulletin* **94**(5) (1983), 563.
21. E. Bonnet, O. Bour, N.E. Odling, P. Davy, I. Main, P. Cowie, B. Berkowitz, Scaling of Fracture Systems in Geological Media, *Reviews of Geophysics* **39** (3) (2001) 347.
22. O. Bour, P. Davy, Connectivity of Random Fault Networks Following a Power Law Fault Length Distribution, *Water Resources Research* **33** (7) (1997) 1567.
23. L.A. Zadeh, Fuzzy Sets, *Information and Control* **8**(3) (1965) 338.
24. A. Bardossy, L. Duckstein (1995), Fuzzy Rule-Based Modeling with Applications to Geophysical, Biological and Engineering Systems, CRC Press.
25. L. Pan, C.M. Oldenburg, Y.-S. Wu, K. Pruess, Wellbore flow model for carbon dioxide and brine, *Energy Procedia*, GHGT9 conference, Nov. 16-20, 2008, Washington DC. LBNL-1416E.
26. H. Shi, J.A. Holmes, L.J. Durlofsky, K. Aziz, L.R. Diaz, B. Alkaya, G. Oddie, Drift-flux modeling of two-phase flow in wellbores, *Soc. Pet. Eng. J.* **10** (2005) 24.
27. K. Pruess, C.M. Oldenburg, G.J. Moridis. TOUGH2 User's Guide Version 2. E. O. Lawrence Berkeley National Laboratory Report LBNL-43134, November 1999.
28. K. Pruess, N. Spycher, ECO2N – A fluid property module for the TOUGH2 code for studies of CO_2 storage in saline formations, *Energy Conversion and Management* **48** (2007) 1761.
29. J.P. Brill, H. Mukherjee, *Multiphase Flow in Wells*. Monograph Volume 17, SPE Henry L. Doherty Series, 1999.
30. F.K. Chow, P.W. Granvold, C.M. Oldenburg, Modeling the effects of topography and wind on atmospheric dispersion of CO_2 surface leakage at geologic carbon sequestration sites, *Energy Procedia*, GHGT-9 conference, Nov. 16-20, 2008, Washington DC., LBNL-1420E.
31. N. Zuber, J.A. Findlay, Average volumetric concentration in two-phase flow systems, J. Heat Transfer ASME, 87(4), 453-468, 1965.
32. M. Xue, K.K. Droegemeier, V. Wong: The Advanced Regional Prediction System (ARPS): A multi-scale nonhydrostatic atmospheric simulation and prediction model. Part I: Model dynamics and verification, *Meteorol. and Atmos. Phys*. **75** (2000) 161.
33. M. Xue, K.K. Droegemeier, V. Wong, A. Shapiro, K. Brewster, F. Carr, D. Weber, Y. Liu, D. Wang: The Advanced Regional Prediction System (ARPS): A multi-scale nonhydrostatic atmospheric simulation and prediction tool. Part II: Model physics and applications, *Meteorol. and Atmos. Phys.* **76** (2001) 143.
34. R.E. Britter, Atmospheric Dispersion of Dense Gases, *Annual Reviews of Fluid Mechanics* **21** (1989) 317.